

pubs.acs.org/JACS Article

# Superradiance and Directional Exciton Migration in Metal—Organic Frameworks

Sreehari Surendran Rajasree,<sup>#</sup> Jierui Yu,<sup>#</sup> Saied Md Pratik, Xinlin Li, Rui Wang, Amar S. Kumbhar, Subhadip Goswami, Christopher J. Cramer, and Pravas Deria\*



Cite This: J. Am. Chem. Soc. 2022, 144, 1396-1406



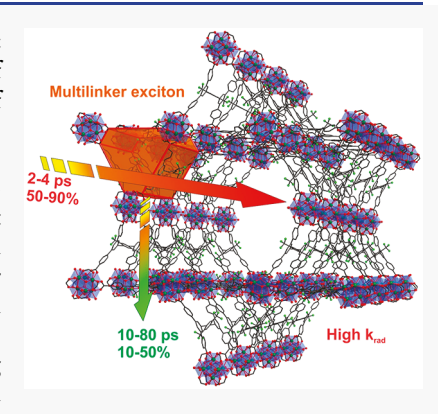
**ACCESS** 

III Metrics & More

Article Recommendations

s) Supporting Information

**ABSTRACT:** Crystalline metal—organic frameworks (MOFs) are promising synthetic analogues of photosynthetic light-harvesting complexes (LHCs). The precise assembly of linkers (organic chromophores) around the topology-defined pores offers the evolution of unique photophysical behaviors that are reminiscence of LHCs. These include MOF excited states with photoabsorbed energy that is spatially dispersed over multiple linkers defining the molecular excitons. The multilinker molecular excitons display superradiance—a hallmark of coupled oscillators seen in LHCs—with radiative rate constant ( $k_{\rm rad}$ ) exceeding that of a single linker. Our theoretical model and experimental results on three zirconium MOFs, namely, PCN-222(Zn), NU-1000, and SIU-100, with similar topology but varying linkers suggest that the size of such molecular excitons depends on the electronic symmetry of the linker. This multilinker exciton model effectively predicts the energy transfer rate constant; corresponding single-step exciton hopping time, ranging from a few picoseconds in SIU-100 and NU-1000 to a few hundreds of picoseconds in PCN-222(Zn), matches well with the experimental data. The model also predicts the



anisotropy of exciton displacement with preferential migration along the crystallographic *c*-axis. Overall, these findings establish various missing links defining the exciton size and dynamics in MOF-assembled linkers. The understandings will provide design principles, especially, positioning the catalysts or electrode relative to the linker orientation for low-density solar energy conversion systems.

## **■ INTRODUCTION**

The elegant protein-assembled arrays of chlorophyll and other photosynthetic pigments define the light-harvesting antenna in the light-harvesting complex (LHC). These antenna arrays not only absorb photons and deliver the excitation energy to the special pair (reaction center) initiating the charge transfer but operate in a way that can effectively drive subsequent multielectron redox chemistry (e.g., water oxidation at PS-II and CO<sub>2</sub> reduction at PS-I). Some of these design principles have inspired a wide range of developments including synthetic molecular assemblies that target functioning with comparable efficiency. 1-8 Precise positioning of the pigments with optimal relative distance and orientation and a high degree of spectral overlap (donor fluorescence and acceptor absorption bands) are some of the critical factors behind an efficient Förster-like resonance energy transfer (FRET) process. One salient feature of the natural LH antenna is the evolution of correlated ensembles possessing macroscopic transition dipoles. The corollary of these correlated oscillators is a cooperative emission with a radiative rate constant  $(k_{rad})$  exceeding that determined for their respective monomeric building blocks entailing large photon absorptivity and efficient directional exciton migration (through the alignment of their larger transition dipoles).

Achieving such functionalities in artificial chromophore assemblies has been difficult mainly due to the challenge of supramolecular synthesis of ordered chromophores in high concentrations that can circumvent various unproductive exciton recombination processes. 9-17 We and others have investigated crystalline metal—organic frameworks (MOFs)<sup>18-26</sup> as a unique platform to engineer energy-transducing functionalities. The MOF offers a scalable modular scaffold where interchromophore distance and orientation can be fine-tuned by its topology-defined structures. Besides various common benefits that a porous composition would offer, MOF pores can be tailored via various postsynthesis processes to install the desired photo- and/or redox-active functionalities to design synthetic LH systems.

Our work on MOF-assembled chromophores has established that the excited states in MOF can span over multiple linkers producing molecular excitons (i.e., spatially dispersed

Received: November 12, 2021 Published: January 14, 2022





photon energy).<sup>27</sup> A multilinker model also implies that the photogenerated excitons can effectively sample hundreds of linkers with a reasonably fewer number of hopping events (compared to an ultrafast time it would need for a single linker localized exciton). Nevertheless, the spatial extent of the electron—hole correlation within these molecular excitons remains unestablished and, therefore, has been a barrier to understanding the exciton migration and the key parameters that control the subsequent dynamics and direction. In this regard, we have also shown that assembling linkers with low electronic symmetry in an anisotropic framework can significantly improve energy transfer.<sup>28</sup> In a FRET-like process with

$$k_{\rm FRET} = 2\pi J^2 \Theta / \hbar \tag{1}$$

where J (eV) is the interchromophoric electronic coupling and  $\Theta$  (eV<sup>-1</sup>) represents the overlap integral between the areanormalized donor fluorescence and acceptor absorption bands; <sup>29–33</sup> an extended transition dipole of the linker molecules improves the  $\Theta$ , <sup>34</sup> and their anisotropic alignment along one crystalline axis (MOF-topology defined) improves the J. <sup>33</sup> Nevertheless, the efficacy of this strategy was not established in terms of anisotropic exciton displacement.

In this study, we present a combined understanding of the correlated oscillators in anisotropic MOFs that display superradiance  $(\sigma_r)$  in vectorial exciton migration;  $\sigma_r$  is defined by

$$\sigma_{\rm r} = k_{\rm rad}^{\rm MOF}/k_{\rm rad}^{\rm L} = |\mu_{\rm MOF}/\mu_{\rm L}|^2 \tag{2}$$

where  $\mu$  is the transition dipole moment and  $k_{\rm rad}$  is the radiative rate constant ( $k_{rad}$  can also be measured from the ratio between emission quantum yield (QY) and lifetime; vide infra) and facilitates efficient energy transfer (EnT). For this, we take three well-established zirconium MOFs—namely, PCN-222(Zn),<sup>35</sup> NU-1000,<sup>36</sup> and SIU-100<sup>28</sup>—constructed by interconnecting a  $D_{4h}$ -symmetric TCPP(Zn), a  $C_{2v}$ -symmetric tetraphenylpyrene (TBAPy), or an elongated, C2-symmetric 1,4-bis(phenyleneethyne)phenylene (PEPF) linker with 8connected Zr<sub>6</sub>-oxo nodes (Figure 1). The mesoporous PCN-222(Zn), NU-1000 (csq), and SIU-100 (xly) provide comparable structural scaffolds with hexagonal ( $d \approx 32$  Å, considering a planar PEPF linker disregarding the rotational flexibilities of the central -Ph(CF<sub>3</sub>)<sub>2</sub> moiety in SIU-100) and triangular 1D pore channels propagating along the crystallographic c-axis. These MOFs present node-sharing triangularshaped linker arrays. The time-dependent density functional theory (TDDFT) computation on such single and multiple adjacent triangular arrays (along the ab-plane or c-axis) suggests that the electron-hole correlation spans over these triangular arrays defining the molecular exciton site. The TDDFT-computed transition-dipole moments for these triangular arrays were used to estimate and predict the  $k_{\text{FRET}}$ that matches with the experimental data obtained from the respective Stern-Volmer (SV)-type amplified emission quenching experiments (using postsynthetically installed ferrocene-carboxylate as redox quencher within the pores of these MOFs). Steady-state and transient fluorescence spectroscopic data highlight that these MOFs display superradiance  $(\sigma_{\rm r})$  with  $k_{\rm rad}$  exceeding that measured for the corresponding solution-dissolved linkers; MOFs with larger  $\sigma_r$  show efficient EnT. The findings presented here can be translated into the future development of porous artificial light-harvesting

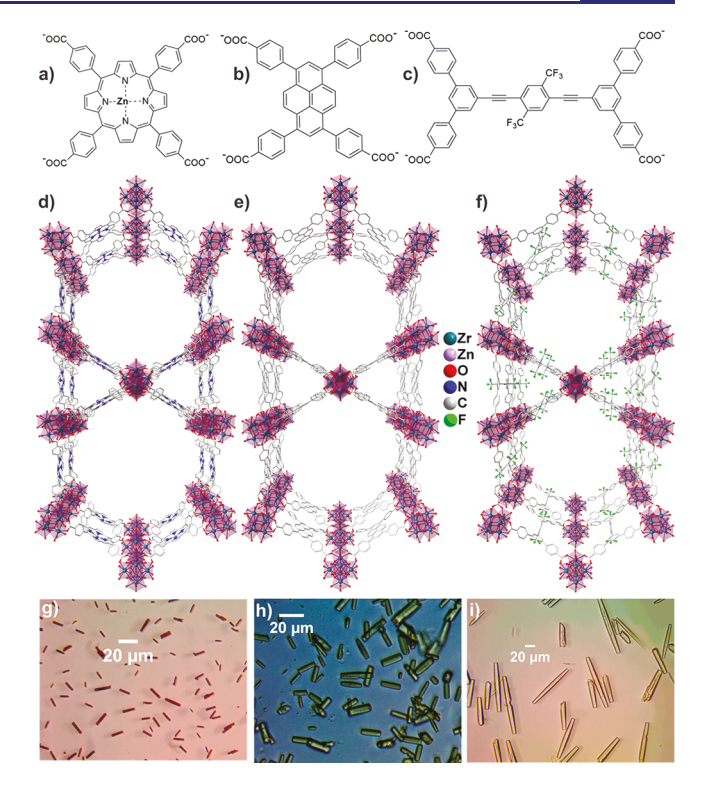


**Figure 1.** Structures of deprotonated (a) TCPP(Zn), (b) TBAPy, and (c) PEPF linkers and their corresponding MOFs (d) PCN-222(Zn), (e) NU-1000, and (f) SIU-100. The respective optical microscopic images (g—i) highlight their anisotropic needle-shaped morphology.

systems, as efficient and highly anisotropic exciton displacement is critical for delivering the photogenerated excitons to the catalytic sites or the exciton splitting site for energy conversion.<sup>37</sup>

## ■ METHODS SECTION

**Materials.** All solvents used for spectroscopic studies, including 2-methyltetrahydrofuran (MeTHF), 3-methylpentane (MePent), and dimethylformamide (DMF), were purchased from Sigma-Aldrich and used as received. Details of MOF synthesis and characterizations are presented in the Supporting Information (Supporting Information section B–D).

**Instrumentation.** The quencher (ferrocene, Fc) distributions within MOF crystals, especially for those with low Fc/linker loading ratio, were examined using (a) confocal microscopy and (b) highangle annular dark-field (HAADF) images and energy-dispersive X-ray spectroscopy (EDS) elemental mapping. A Lecia SP8 confocal fluorescence microscope was used for imaging emission intensity along with the MOF crystals: all the MOF samples were excited with a 405 nm laser, and emissions at the central z-stack of each crystal were collected using the specific filter to choose the probe wavelength range, whereas HAADF and EDS elemental mappings images were collected using a Thermofisher Talos F200X STEM.

Diffused transmittance spectra for MOF samples were measured using a JASCO V-670 UV–vis–NIR spectrophotometer outfitted with a 60 mm BaSO<sub>4</sub>-coated integrating sphere, where the MOF films were placed at the exterior entry point of the sphere to reduce the scattering. An Edinburgh FS5 spectrofluorometer was used to record the steady-state emission spectra (with a front-face sample module) and the absolute emission QY, henceforth denoted as  $\varphi_{\rm em}$  (with a 150 mm BaSO<sub>4</sub> integrating sphere). The crystalline powder samples were immersed in desired solvents packed in Teflon-sealed quartz capillary tubes for measurement, and the spectra were corrected using the instrumental correction functions for both excitation and emission light signals.  $^{27,37}$  Fluorescence lifetimes were determined by fitting the

respective emission decay profiles recorded on an Edinburgh Lifespec II picosecond time-correlated single-photon counting (TCSPC) spectrophotometer equipped with a Hamamatsu H10720-01 detector and a 403 or 507 nm picosecond pulsed diode laser as TCSPC excitation source (using the instrument response function measured separately). Instrumental control, kinetic data collection, processing, and fitting were performed using F980 software. Sample preparations and instrumental details along with experimental conditions are described in the SI (section A).

Computational Methods. The energy and oscillator strength of electronic excitations were computed on single and adjacent (node shared) triangular arrays. The structures of the corresponding arrays were extracted from the crystallographic coordinates (Figure 6a,b and Figure 7a,b). In these calculations, the metal-oxo nodes were removed and a proton was added to each carboxylate group to achieve charge neutrality.<sup>27</sup> The mono- and bis-triangular arrays then underwent constrained optimization, where the terminal carboxylate moieties were fixed to their crystallographic coordinates, allowing the linkers to maintain their relative positions as defined by the respective framework topology. Oscillator strengths and their corresponding transition energies and densities were obtained via TDDFT computation of 30-40 excited states using the HSEH1PBE functional and 6-311g(d,p) basis set except for PCN-222(Zn)-based arrays, where the 6-31g(d,p) basis set was used (see SI section F). Transition density matrix (TDM) analysis was performed using Multiwfn 3.7 software, and contour maps were plotted in MATLAB.<sup>38</sup>

### RESULTS AND DISCUSSION

Compared to the symmetric TCPP(Zn) that manifests a weak Q-band-derived lowest energy transition,<sup>39</sup> the TBAPy and PEPF linkers entail large x-polarized transition dipoles culminating in higher  $\Theta^{40,41}$  as well as higher  $k_{\rm rad}$  as

$$k_{\rm rad} = \frac{16\pi^3}{3\epsilon_o h c^3} \left[ \frac{n^3}{\epsilon_r} \right] E^3 |\mu|^2 = \frac{\varphi_{\rm em}}{\tau_{\rm em}}$$
(3)

where  $\epsilon_r$  is the relative dielectric constant, n is the refractive index of the bulk solution,  $\epsilon_0$  is the permittivity of free space, c is the velocity of light, h is Planck's constant, and E is the transition energy.  $^{42,43}$  Here,  $au_{\rm em}$  is the emission lifetime.

And  $\mu$  can be calculated from

$$\mu = \langle e \cdot r \rangle \tag{4}$$

r is the transition dipole length, where

$$r^{2}(\mathring{A}) = \frac{f}{2500G\overline{v}} = \frac{\varepsilon_{\text{max}}d\overline{v}}{2500G\overline{v}}$$
 (5)

Here, f is the oscillator strength and can be approximated as the area defined by the molar extinction coefficient  $\varepsilon_{\text{max}}$  in M<sup>-1</sup> cm<sup>-1</sup> and the full width at half-maximum,  $d\overline{v}$  in cm<sup>-1</sup>, obtained from the UV-vis absorption band; G is the degeneracy of spectroscopic state, and  $\overline{v}$  is the wavenumber corresponding to the absorption peak.44 Experimental transition dipole moments,  $\varphi_{\rm em}$ , and the  $au_{\rm em}$  were determined for DMF-solubilized linkers and are presented in Table 1. The corresponding TDDFT-computed transition dipole moments for the lowest energy transitions of the linker molecules (Table 1) seem to be overestimated consistently by ca. 1.42 times. We will use this factor to scale the TDDFT-computed transition dipole moments determined for the linker arrays in MOFs.4

The studied MOFs fix the linkers along their respective caxis (i.e., around their 1D pore channels); this anisotropic arrangement of a nondegenerate lowest energy transition dipole can render an effective J. Therefore, SIU-100 is expected to be a superior assembly for efficient exciton energy transfer.

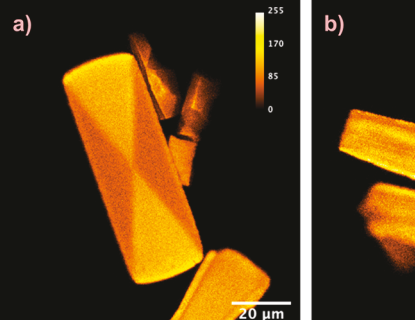
Table 1. Radiative Decay Constant of Linker Molecules with Their Transition Dipole Moments

linker	$\mu_{\rm exp}$ (D)	$\varphi_{\mathrm{em}}$ (%)	$\tau_{\rm em}~({\rm ns})$	$k_{\rm rad}~(\rm ns^{-1})$
$H_4TCPP(Zn)$	$1.74 (2.47^a)$	$3(\pm 0.1)$	1.95	1.54 (±0.1)
$H_4TBAPy$	$6.05 (8.50^a)$	$78(\pm 2)$	1.90	41.05 (±2)
$H_4PEPF$	9.36 (13.39 <sup>a</sup> )	$80(\pm 2)$	3.20	25.00 (±1)

<sup>a</sup>Uncorrected TDDFT-computed  $\mu$  for the S<sub>1</sub> excitations. The  $\mu_{\text{exp}}$ values were determined for the lowest energy transitions. The error in  $\mu_{\rm exp}$  may stem from  $\varepsilon_{\rm max}$  measurement (0.3–1.2%). The  $\tau_{\rm em}$  possess an error of 0.05 ns.

In contrast, only one of the two small degenerate transition dipoles of TCPP(Zn) lies along the *c*-axis (whereas the other is on the ab-plane), culminating in small J. These parameters will have tremendous impacts in defining the respective energy transfer efficiency.

We have probed the EnT and the underlying exciton migration dynamics via an amplified emission quenching experiment using a node-installed electron donor, ferrocene carboxylate, as a redox quencher. 28,46 In this experiment, we probe the extended quenching perimeter of a redox quencher as a measure of exciton hopping efficiency. The eightconnected Zr6-oxo nodes were exploited to install ferrocenecarboxylate using well-established solvent-assisted ligand incorporation (SALI) with varying Fc/linker ratios (see SI section B3). 47-51 The extent of Fc loading and distribution in MOF crystals were quantified using SEM-EDS analysis (see SI section D1). The even distribution of the Fc, regardless of its loading concentration—a critical parameter to systematically probe the exciton dynamics—was probed using confocal microscopy. For samples with a low (~0.05) Fc/linker loading ratio, Figures 2 and S8a highlight an even emission intensity



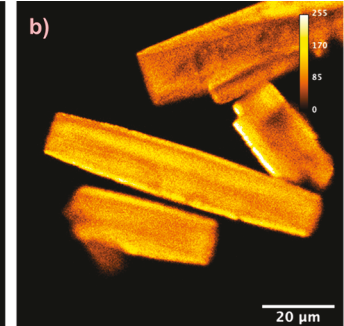
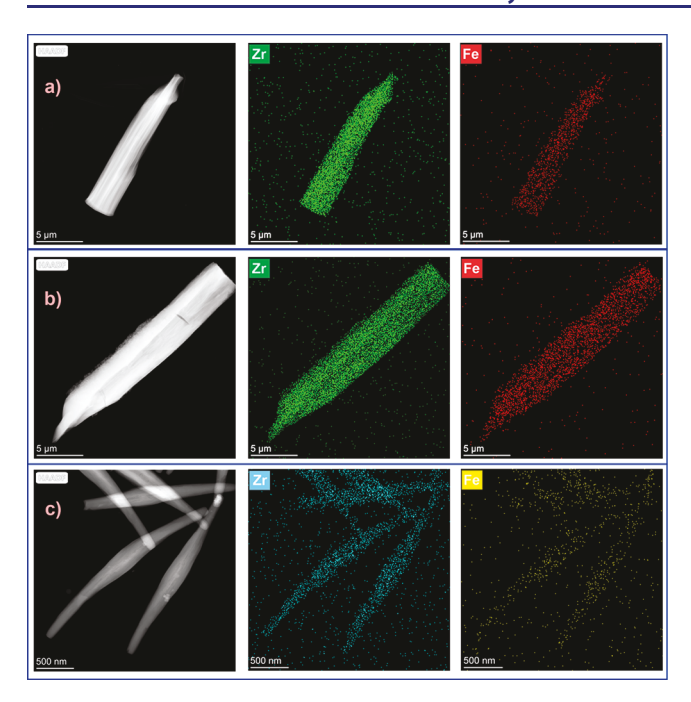


Figure 2. Confocal microscopy image of (a) Fc@NU-1000 and (b) Fc@SIU-100 highlighting evenly distributed emission profiles from the crystallites with ca. 0.05 Fc/linker loading.

profile. These data suggest that the SALI-installed Fc moieties are not concentrated to any specific zone (like at the outer surface) even at low loading conditions. To further "visualize" the extent of spatial Fc distribution within the MOF crystallites, elemental mapping over their HAADF images (Figure 3 and S8b) was collected; these data display high uniformity of the Fc installation via SALI.

These Fc-decorated MOF samples show a monotonic decrease in the emission intensity with an increase in Fc loading (see SI Appendix for the relevant photophysical data); the relation can be analyzed using the SV relationship:



**Figure 3.** HAADF images and EDS elemental mapping of (a) Fc@NU-1000, (b) Fc@SIU-100, and (c) Fc@PCN-222(Zn) showing the uniform distribution of Fe (right column) over Zr (middle column) at a low Fc loading (~0.05 Fc/linker).

$$\frac{\varphi_{\rm em}^0}{\varphi_{\rm em}^{\rm R}} = 1 + K_{\rm SV}[{\rm R}] \tag{6}$$

where  $\varphi_{\rm em}^0$  is the intrinsic (i.e., without quencher) QY and  $\varphi_{\rm em}^{\rm R}$  is QY at a redox quencher concentration of [R] (presented in terms of the Fc/linker as determined by SEM-EDS elemental analysis; SI section D1). Since the Fc quencher is fixed at the Zr-oxo node, close to the linkers, the emission quenching will probe the diffusion of the molecular exciton (instead of the quencher) and the quenching process would relate  $K_{\rm SV}$  to the number of chromophores the exciton visits within its lifetime.  $^{33,46,50-52}$ 

The analysis of the quenching data (Figure 4) revealed that PCN-222(Zn) manifests a small  $K_{\rm SV}$  value of 12 compared to SIU-100 ( $K_{\rm SV}$  = 150). These data agree well with the above prediction for SIU-100 (xly topology) being superior assembly facilitating the exciton to sample order-of-magnitude more linkers compared to that in PCN-222(Zn) (csq topology). If we assume the molecular excitons are localized over just a single linker, the total number of hops—considering an anisotropic, one-dimensional hopping-that an exciton would make is 5625 for SIU-100 and 36 for PCN-222(Zn) (see also SI section G1).54 Considering their respective lifetimes, the single-step hopping time required for SIU-100 will be on the order of 160 fs ( $k_{\text{hop}} = 0.63 \times 10^{13} \text{ s}^{-1}$ ), which is at least an order of magnitude faster than what is observed in natural LH arrays. The corresponding time for PCN-222(Zn) was estimated to be ~35 ps, given the weak coupling and small transition dipole; nevertheless, for both the MOFs, the singlestep hopping rates are significantly overestimated. NU-1000, on the other hand, displays  $\gtrsim 2 \times$  the  $K_{SV}$  compared with SIU-100 despite a smaller transition dipole moment of the TBAPy linker compared with PEPF (Table 1). Note that a  $K_{SV}$  of 360 would require a single-step hopping time of 30 fs ( $k_{\text{hop}} = 3.3 \times$ 10<sup>13</sup> s<sup>-1</sup>). In all these cases, the general trend of considerably

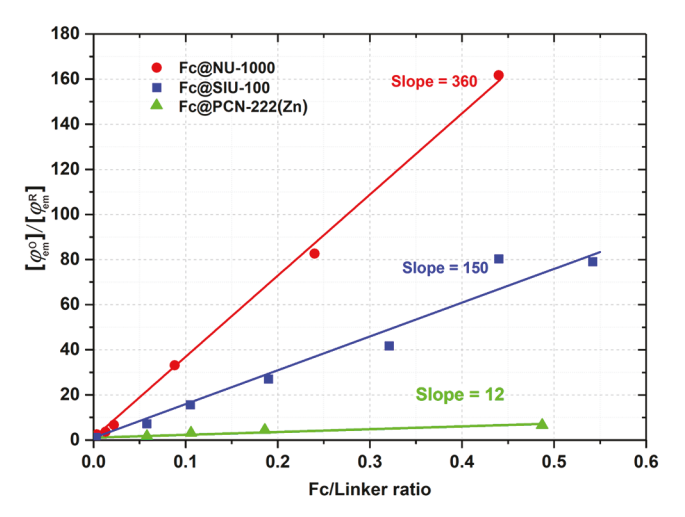


Figure 4. Stern—Volmer plot of PCN-222(Zn) (green), NU-1000 (red), and SIU-100 (blue) against the extent of node-installed ferrocene-carboxylate per linker. For PCN-222(Zn) samples,  $\varphi_{\rm em}^0$  values were measured in MePent solvent; MeTHF solvent was used for SIU-100 and NU-1000 samples (see SI section E3).

short single-step hopping time is stemming from our assumption that the molecular exciton is localized over a single linker. With this assumption, the SV analysis for the quenching efficiency was performed against the number of quenchers per linker. This would mean that for a single linker-based exciton a large number of hopping events are required to sample hundreds of linkers within the exciton lifetime. Therefore, such an analytical model needs to be amended with a model that accommodates the idea of spatially dispersed molecular excitons spanning over multiple linkers.

We have reported that the electronic transitions including the  $(S_1 \rightarrow S_0)$  emissions commonly feature broad spectral envelopes (fwhm \$\ge 3500 \cdot cm^{-1}) compared to their solution-dissolved linkers. Possible contributions from crystal vibration and related phonon-exciton coupling can be excluded as the spectra recorded at systematically lowered temperature including frozen glassy solvents at 77 K (Figure S9) did not display any narrower line width. Since no new transition nor any shift in transition energy—due to an excitedstate complex (e.g., excimer or CT-type complex) formation was observed in the respective time-resolved emission spectra, we infer that such line broadening is inherent to these solid compositions.<sup>55</sup> Such line broadening can occur in a system where the excited states are shared by multiple molecular pigments, like our system, where excitons span over multiple linkers.<sup>56</sup> In related studies, we have examined such possibilities by probing excited-state features of several intuitively selected linker arrays.<sup>27</sup> In this work, we examine the triangular linker arrays in the csq/xly MOFs as the possible molecular exciton site since this smallest array defines a proximally positioned (center-to-center distance ~10 Å) assembly suitable to form a coupled oscillator and define a molecular exciton. If so, such correlated oscillators will entail (a) an e-h correlation among all three linkers within the array and (b) a transition dipole moment that is larger than that of an individual linker. These fundamental features will ensure that the MOF assembled linkers should display a discernible superradiance ( $\sigma_r > 1$ ; eq 2), and these multilinker excitons should explain its hopping dynamics and anisotropic energy transfer.

To glean a better picture of some of the unique excitonic properties in these frameworks,  $^{51,57}$  we have constructed triangular arrays—namely, PCN-222(Zn)t, NU-1000t, and SIU-100t—solely based on three corresponding linkers without the  $\rm Zr_6$ -oxo node. We and others have shown that these  $\rm [Zr_6(\mu_3\text{-O})_4(\mu_3\text{-OH})_4(-OH)_4(-OH_2)_4]^{8+}$  nodes are optoelectronically inert with a large electronic bandgap relative to any aromatic linkers used here.  $^{27,47,58,59}$  These nonexhaustive models are constructed from the crystallographic coordinates and were subjected to restricted optimizations, where the carboxylates were protonated and fixed at the crystallographic coordinates.

TDDFT-computed absorptive transition energies and oscillator strengths for these triangular arrays were used to construct the simulated absorption spectra (Figure 5 bottom

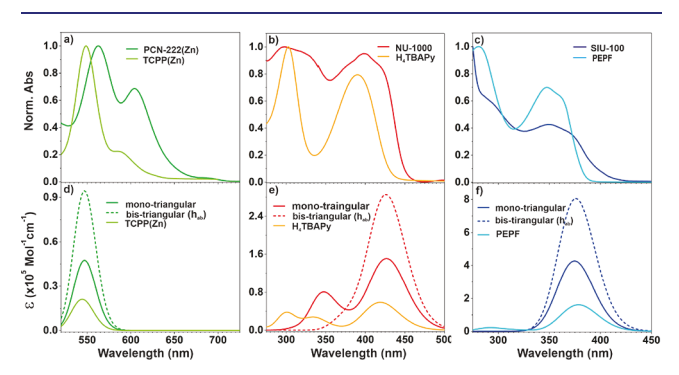


**Figure 5.** Absorptive electronic transitions of the MOFs and linkers: Top row displays the experimental spectra of (a) PCN-222(Zn), (b) NU-1000, and (c) SIU-100 along with their respective linkers; the bottom row (d, e) displays respective simulated absorption spectra generated via Gaussian reconvolution (fwhm =  $3000~\text{cm}^{-1}$ ; for PCN-222(Zn)t an fwhm =  $1000~\text{cm}^{-1}$  was used) of the TDDFT-computed oscillator strengths and transition energies for the mono- and bistriangular arrays of MOFs relative to their single linkers. Note that for larger systems the computed spectra present only the lowest energy transition.

row); these spectra match well with the experimental data collected for the (solid) MOF films and the solution-dissolved linkers. The corresponding  $\mu$  values (corrected for the overestimation using the 1.42× scaling factor seen for the single-linker computation; vide supra), later used for  $k_{\text{FRET}}$ estimation, reveal that the triangular arrays indeed entail a ca. 1.5 times larger value compared to their individual linkers. Excitonic properties of the model compounds were examined by analyzing their respective TDMs, which map atomistic electron-hole correlations during the optical excitations.<sup>60</sup> In these TDM contour maps, the diagonal densities or the diagonal size  $(N_d)$  signifies the distribution of the excitonic center-of-mass. In other words,  $N_d$  represents the number of atoms that the optical excitation spans, i.e., the excitonic wave function. In contrast, the off-diagonal size  $(N_{\rm c})$  defines the degree of e-h coherence, i.e., the exciton size.  $^{17,61,62}$  If  $N_{\rm t}$  is the total number of atoms involved in a given optical excitation (e.g.,  $S_0 \rightarrow S_1$ ), then for a delocalized and loosely bound exciton,  $N_{\rm d}$  =  $N_{\rm t}$  =  $N_{\rm c}$ . However, for organic pigments and related assemblies, the molecular excitons have significant binding energy. Therefore,  $N_c \neq N_d$ , where  $N_d$  may be large, and for our three or six linkers-based models, it may span over all the atoms  $(N_t)$ . Therefore, we consider the extent of the offdiagonal density span  $(N_c)$ , in the respective TDM, as the exciton size. Figure 6c,d,e highlight the TDM plots relevant to

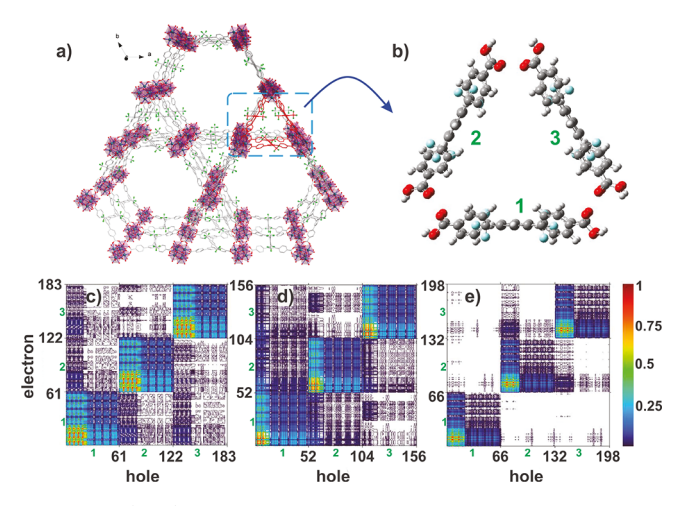


**Figure 6.** (a, b) DFT-optimized structure showing the triangular linker array for SIU-100. Contour plots of TDMs corresponding to the first bright excited state  $(S_1)$  of monotriangular unit (c) PCN-222(Zn)t, (d) NU-1000t, and (e) SIU-100t. These plots represent electron—hole correlation over each atom (the axis scales represent the atom index) during an optical excitation. The color bar represents the normalized atomic transition densities.

the  $S_1$  states for these triangular linker arrays. These plots display diagonal densities over all three linkers of these arrays—appearing as "box-shaped" blocks over the aromatic cores as well as the side phenyls—indicating that all the linkers contribute to the excitonic wave functions. Besides these "box-shaped" diagonal densities, the nonzero off-diagonal densities for the  $S_1$  states highlight an e—h correlation among all three linkers (with a size of ~2.7 nm). The low off-diagonal density (~10%) is expected for such weakly coupled arrays, resulting in a transition dipole moment that is only ~1.5× higher relative to the monomer (instead of a maximum possible value of 3  $\mu_L$  for a strongly coupled parallel arrays).

Given that the size of the excitons entirely spans our three-linker models, we wanted to expand the size of our model. As discussed above, if these triangular arrays represent the molecular excitonic sites, incorporating multiple such adjacent triangular arrays would simply scale the resulting oscillator strength. A series of hexa-linker arrays was similarly constructed from the crystallographic coordinates. The first series is from two adjacent triangular blocks positioned on the *ab*-plane and connected through one Zr-oxo node and named PCN-222(Zn)h<sub>ab</sub>, NU-1000h<sub>ab</sub>, and SIU-100h<sub>ab</sub> (Figure 7a,b). The TDDFT-computed transitions and corresponding simulated spectra are presented in Figure 5; these spectra simply highlight ca. doubly intense peaks than their monotriangular analogues.

The corresponding TDM plots (Figure 7c,d,e), relevant to the  $S_1$  state transitions, for these hexa-linker arrays also display similar diagonal densities over all six linkers in the arrays—appearing as blocks over all six linkers—as all six linkers fixed at the ab-plane contribute to the excitonic wave functions for the optically allowed  $S_1$  state. Nevertheless, the nonzero off-diagonal densities form the "box-shaped" maps spanning over three linker ensembles (linker 1, 2, and 3 or 4, 5, and 6 form an ensemble), confirming the extent of the e—h correlation. The respective oscillator strengths (i.e., for  $S_0 \rightarrow S_1$  transitions) computed for these hexa-linker bis-triangular arrays are presented in Figure 8 relative to their corresponding monotriangular arrays. These data suggest that the bis-triangular

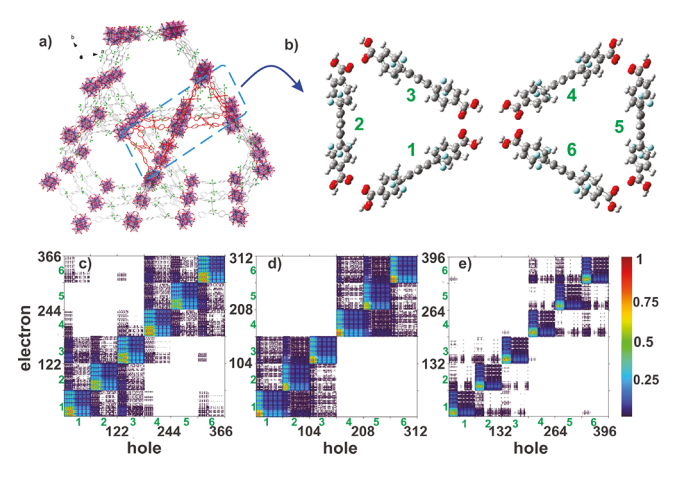


Figure 7. (a, b) DFT-optimized structure showing the bis-triangular array (on the ab-plane) for SIU-100. Contour plots of transition density matrices (TDMs) corresponding to the first bright excited state (S<sub>1</sub>) of bis-triangular (c) PCN-222(Zn), (d) NU-1000, and (e) SIU-100 models. The atomic numbers were also marked with the respective linker numbers shown in panel (b). The color bar represents the normalized atomic transition densities.

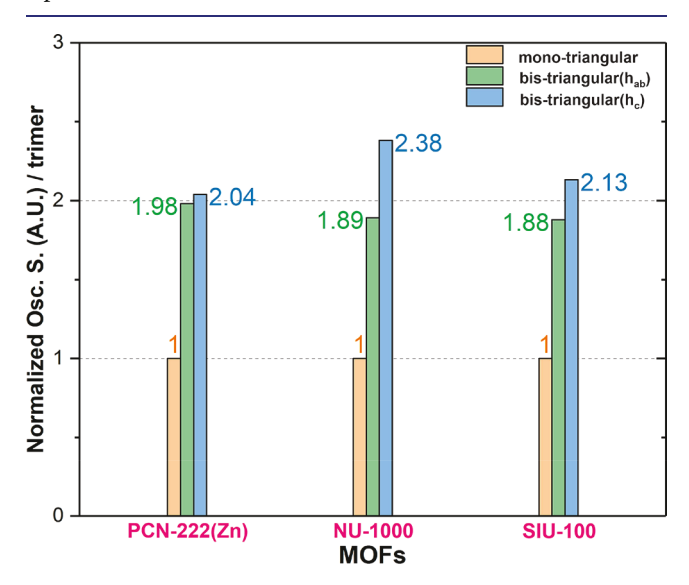


Figure 8. Oscillator strengths of different bis-triangular arrays computed for their  $S_0 \rightarrow S_1$  transition, normalized to their respective mono-triangular unit.

arrays entail twice the oscillator strength compared to that of their mono-triangular arrays. A second series of hexa-linker arrays was also constructed where two adjacent triangular blocks are positioned along the c-axis (connected through three shared Zr-oxo nodes), forming PCN-222(Zn)h, NU-1000h<sub>ct</sub> and SIU-100h<sub>ct</sub>. TDDFT computation on these models also rendered oscillator strengths that are ca. twice compared to the corresponding mono-triangular arrays (Figures 5, 8). These findings support that the triangular arrays represent correlated ensembles of the molecular exciton sites. The size of such coherence spans over about four bacteriochlorophyll monomers in the natural LHC found in, for example, Rhodobacter sphaeroides. 43,64

Coming back to the exciton-hopping dynamics and direction, the amplified quenching experimental dataoriginally presented in Figure 4-can now be reanalyzed with this multilinker exciton model. For that, a modified SV

quenching is plotted against Fc/exciton site (Figure 9). Likewise, the  $K_{SV}$  represents the number of excitonic sites

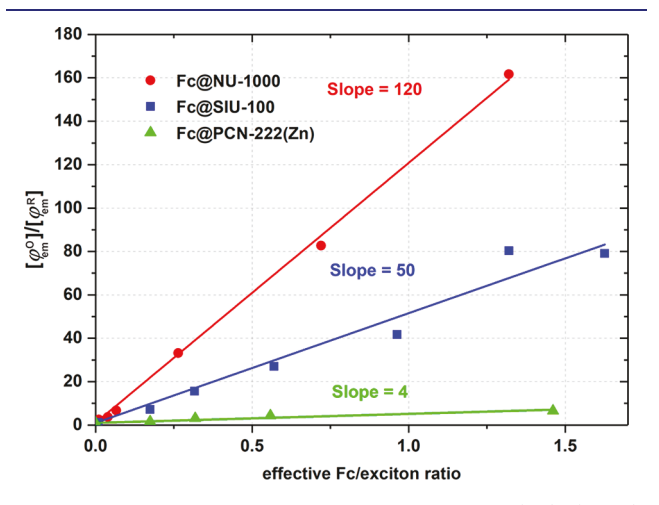
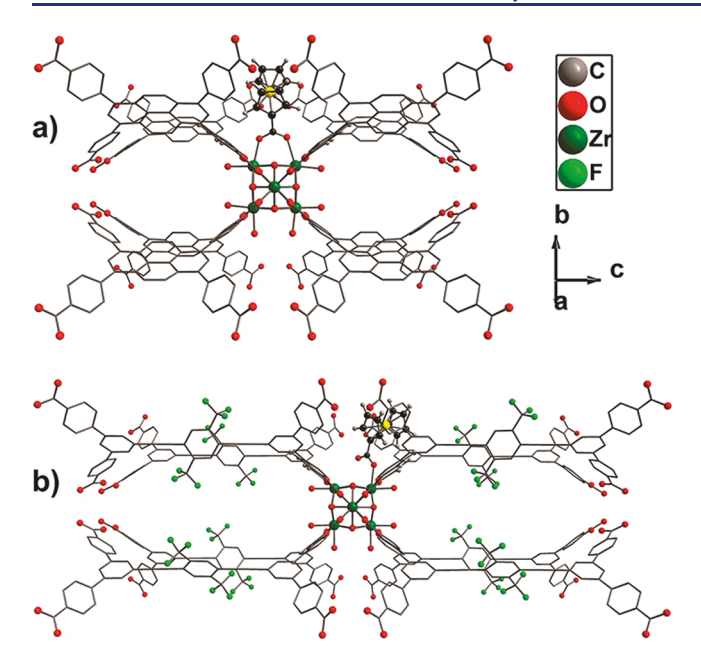


Figure 9. Modified Stern-Volmer plot of PCN-222(Zn) (green), NU-1000 (red), and SIU-100 (blue) against the node-installed ferrocene-carboxylate per exciton site.

visited by the exciton. Considering one-dimensional exciton hopping, for SIU-100, the  $K_{SV}$  of 50 would translate into ~625 hops, whereas PCN-222(Zn) would manage only four hops within its lifetime. 52 Therefore, the single-step hopping time needed for SIU-100 and PCN-222(Zn) is 1.4 ps ( $\approx$  0.89 ns/ 625) and 175 ps ( $\approx$  0.7 ns/4), respectively. While this multilinker exciton model describes a general trend in the exciton hopping, NU-1000 manifested a  $K_{SV}$  of 120, which is slightly more than double compared to what is seen for SIU-100. We believe this anomalous behavior observed in NU-1000 can, for the most part, be explained by considering the unique position of the ferrocene-carboxylate redox quencher compared to other MOFs. This stems from the extent of steric hindrance at the Fc-installation site of the Zr-oxo SBU—posed by the orientation of the carboxy-phenyl groups (relative to the Zr<sub>6</sub>-oxo cluster and the aromatic core) of the linkers—such that the Fc-COO can be anchored in an  $\eta^2$ - $\mu^2$  mode where it bridges two adjacent Zr ions (replacing a hydroxo and an aqua ligand) or in a monodentate fashion (replacing only one hydroxo ligand). Between the two places—one protruding to the hexagonal channel and the other behind the node along the c-axis (c-pocket), NU-1000 installs Fc-COO through a  $\eta^2$ - $\mu^2$ bridging mode at its hexagonal channel. This mode of binding positions the Fc at an equal distance from two adjacent exciton sites.65 In contrast, the Zr-oxo SBU of SIU-100 (and PCN-222(Zn)) installs the Fc-COO through a monodentate binding mode, allowing it to bend/tilt toward one exciton site. The optimized (semiempirical) structures displaying these two different binding modes are presented in Figure 10 (see SI section F2). We reason that this unique Fc positioning should double the quenching probability in NU-1000, and therefore, accounting for this effect, we can consider an effective  $K_{SV}$  of 60 for NU-1000, culminating in a single-step hopping time of  $\sim$ 1.1 ps (1 ns/900). In two recent publications, we established that such an  $\eta^2 - \mu^2$  binding mode even for sterically demanding carboxy-appended porphyrin, <sup>37,66</sup> where an electron-deficient dinitrobenzene bound to some extent in a monodentate mode,  $^{67}$  manifests a smaller  $K_{\rm SV}$ .  $^{46}$  This postulation was further proved by using a small, nonbound, quencher such as trimethylamine (TEA), as described in SI section G2. Under



**Figure 10.** Optimized structure showing the position of Fc-COO at the Zr-SBU relative to four possible exciton sites of NU-1000 and SIU-100. The difference stems from the carboxylate binding mode as allowed by the sterics provided by the four carboxyphenyls of the linkers.

similar conditions and assuming chemical diffusion of TEA to be similar in NU-1000 and SIU-100, we find SIU-100 and NU-1000 showing a comparable  $K_{\rm SV}$ . <sup>68</sup> A small part behind a high  $K_{\rm SV}$  (i.e., more than just double) in NU-1000 can be attributed to the contribution of underlying EnT occurring from the excitation of its *y*-polarized transition: in NU-1000, the *y*-polarized transition ( $\sim$ 0.35 eV blue to the lowest energy  $\kappa$ -polarized transition) holds a significant oscillator strength and can be simultaneously excited (see SI section H2 for relevant experimental and theoretical probes).

With the multilinker excitonic sites defined, we wanted to probe if the corresponding TDDFT-computed transition dipole moments (for their respective lowest energy transitions) can effectively explain the exciton-hopping dynamics and directions. In a FRET-like process in effect, the  $k_{\rm FRET}$  (eq 1) should predict the site-to-site hopping. For this, various J (eV) values were computed along different directions using

$$J = 0.6251 \frac{\mu_1 \mu_2}{r^3} (\cos \alpha - \cos \beta_1 \cos \beta_2)$$
 (7)

where  $\alpha$  is the angle between transition dipole moments  $\mu_1$  and  $\mu_2$  in Debye (TDDFT computed and corrected for the overestimation using a 1.42× scaling factor obtained for their corresponding free linker; *vide supra*; Table 1); r is the dipole separation in Å, and  $\beta_1$  and  $\beta_2$  are the angles made by each transition dipole with the displacement vector  $(\vec{r})$  connecting the centers of two transition dipoles.

Based on the r, and therefore the J, an exciton at any given position, e.g., point A in Figure 11, has three equal 1D migration probabilities on the ab-plane along the crystallographic  $\vec{a}$ ,  $\vec{b}$ , and  $\vec{a} + \vec{b}$  axes (i.e.,  $\overrightarrow{AD}$  or its equivalent) directions. Arguably, the exciton along the  $\vec{a}$ ,  $\vec{b}$ , or  $\vec{a} + \vec{b}$  axes can efficiently migrate by adopting zigzag paths highlighted with red arrows (through red-colored exciton sites) along the  $\overrightarrow{AB}$  and two other equivalent directions in Figure 11. The

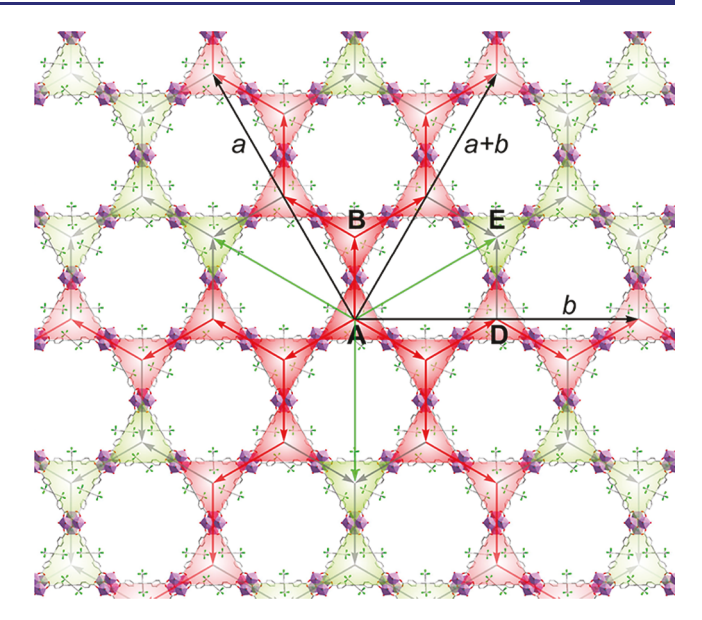


**Figure 11.** Directional exciton migration paths on the ab-plane; the  $\vec{ac}$  direction is perpendicular to this plane and is not shown here.

contribution of a much slower hopping along  $\overrightarrow{AE}$  would be negligible (these are displayed with a green arrow and greencolored exciton sites). Note that once the exciton moves to a new position, it has a similar yet new set of three equal 1D migration probabilities. Nevertheless, the J along AC (i.e., parallel to the  $\vec{c}$ -axis) is expected to be the dominating one given the anisotropic orientation of the transition dipoles along this axis for a head-to-tail coupling. The corresponding parameters are summarized in Table 2, where the  $k_{\text{FRET}}$  values, computed along various directions, clearly suggest that for all three MOFs studied here the exciton displacement is highly preferred along their c-axis. The corresponding single-step hopping times—obtained from summing up various significant  $k_{\text{FRET}}$  values (for each transition dipole,  $k_{\text{FRET}}^{\text{total}} = k_{\text{FRET}}^{\overrightarrow{AC}} + 3 \times k_{\text{FRET}}^{\overrightarrow{AB}} + 3 \times k_{\text{FRET}}^{\overrightarrow{AB}} + 3 \times k_{\text{FRET}}^{\overrightarrow{AB}} - 3 \times k_{\text{FRET}}^{\overrightarrow{AB}}$ match well with those estimated from the modified SV analysis made with a multilinker exciton model (Figure 9).

A relatively smaller (lowest energy) transition dipole moment in NU-1000 did not preclude it from being one of the top-performing frameworks owing to its slightly better  $\Theta$  and a shorter  $d_{(\overrightarrow{AC})}$  compared to that achieved in SIU-100 due to its elongated PEPF linker. The resulting longer  $d_{(\overrightarrow{AC})}$  in SIU-100 impedes the hopping along its dominant migration direction (resulting in a time constant of 1.6 ps).

Given the anisotropic exciton migration, one can estimate that the major fraction of excitons that can be displaced along the  $\overrightarrow{AC}$  direction,  $f(\overrightarrow{AC}) = k_{(\overrightarrow{AC})}/k_{\text{total}}$ , and the absolute number of hops in this preferred direction will be  $f(\overrightarrow{AC}) \times N_{\text{hops}}$  (where  $N_{\text{hops}}$  is the total number of hops). Overall, these results suggest that the multilinker exciton model and their coupled oscillators can be exploited to understand the directional exciton migration where the major fraction ( $\sim$ 90%) of excitons can be displaced over 475 Å in one preferential direction (for NU-1000; Table 3). In general, topologies endowed with 1D pore channels are attractive for efficient EnT-based developments (by parallel orientation of the linkers). In this regard, the csq/xly topological network is

Table 2. Anisotropic Exciton Migration Process and the Comparison of Predicted and Experimental Overall Exciton Migration Rates

MOF	$\Theta (eV^{-1})^a$	$\mu_{\rm cal} \left( {\rm D} \right)^{b}$	d (Å)	J (eV)	$k_{\rm FRET}~({ m s}^{-1})$	$\tau$ (ps)	$ au_{ m av}^{ m pred} \ ( m ps)$	$ au_{ m av}^{ m exp}~( m ps)$
PCN-222(Zn)	0.18	2.42 (ac)	24.23 $(\overrightarrow{AB})$	$26 \times 10^{-5}$	$0.1162 \times 10^9$	8605.0	190 <sup>e</sup>	175
			$17.14 \ (\overrightarrow{AC})$	$-145 \times 10^{-5}$	$3.6142 \times 10^9$	277.0		
			$41.97 \; (\overrightarrow{AD})$	$5 \times 10^{-5}$	$0.0043 \times 10^9$	233 000.0		
			$48.46 \; (\overrightarrow{AE})$	$3 \times 10^{-5}$	$0.0016 \times 10^9$	625 000.0		
		$1.84 \ (ab)^{c,d}$	$24.23 \ (\overrightarrow{AB})$	$26 \times 10^{-5}$	$0.1162 \times 10^9$	8605.0		
			$17.14 \ (\overrightarrow{AC})$	$42 \times 10^{-5}$	$0.3032 \times 10^9$	3298.0		
			$41.97 \; (\overrightarrow{AD})$	$3 \times 10^{-5}$	$0.0016 \times 10^9$	625 000.0		
			$48.46 \; (\overrightarrow{AE})$	$3 \times 10^{-5}$	$0.0016 \times 10^9$	625 000.0		
NU-1000	0.11	9.63 (ac)	$23.73 \ (\overrightarrow{AB})$	$435 \times 10^{-5}$	$0.1990 \times 10^{11}$	50.3	1.4	$1.1^e$
			$16.81 \ (\overrightarrow{AC})$	$-2445 \times 10^{-5}$	$6.2800 \times 10^{11}$	1.6		
			$41.46 \; (\overrightarrow{AD})$	$81 \times 10^{-5}$	$0.0070 \times 10^{11}$	1429.0		
			$47.44$ $(\overrightarrow{AE})$	$54 \times 10^{-5}$	$0.0031 \times 10^{11}$	3333.0		
SIU-100	0.09	15.21 (ac)	23.48 $(\overrightarrow{AB})$	$1117 \times 10^{-5}$	$1.0720 \times 10^{11}$	9.3	1.6	1.4
			25.10 $(\overrightarrow{AC})$	$-1829 \times 10^{-5}$	$2.8800 \times 10^{11}$	3.5		
			$40.69 \; (\overrightarrow{AD})$	$215 \times 10^{-5}$	$0.0400 \times 10^{11}$	252.0		
			46.96 ( $\overrightarrow{AE}$ )	$140 \times 10^{-5}$	$0.0170 \times 10^{11}$	595.0		

 $<sup>^{</sup>a}$ Θ values used here were determined from the absorption and emission spectra of MOFs (not of their linker; see SI section E2).  $^{b}$ Scaled TDDFT-computed transition dipole moment for the triangular model.  $^{c}$ Values shown here are for one of the two degenerate transition dipoles.  $^{d}$ Computed only in the parallel orientation of the transition dipoles (see SI section I); contributions of other orientations on the ab-plane are too small.  $^{c}$ Determined by  $1/k_{\text{FRET}}^{\text{total}}$  where  $k_{\text{FRET}}^{\text{total}}$  is determined for each transition dipole; so for PCN-222(Zn) two  $k_{\text{FRET}}^{\text{total}}$  were taken for degenerate dipoles on the ab-plane.

Table 3. Exciton Displacements along the Preferred  $\overrightarrow{AC}$  Direction in csq and xly MOFs

MOF	fraction of $\overrightarrow{AC}$ hops	displacement in no. of sites	displacement in distance (Å)
PCN- 222(Zn)	0.79	3.2	55
NU-1000	0.91	28.6	480
SIU-100	0.46	17.0	427

unique, as it assembles the linkers anisotropically along its caxis, entailing an effective J, but, most importantly, ensures an ineffective J along the ab-plane due to its large hexagonal channel (the triangular excitonic sites positioned ~24 Å apart between two adjacent (node-sharing) sites). Therefore, the excitons can prefer the anisotropic migration along the  $\overrightarrow{AC}$ direction. To visualize this postulation, PCN-223(Zn), a topologically different MOF with 1D pores, was considered; with its edge-sharing triangular sites, a large J along its ab-plane can be expected to drive ~80% of the excitons along the abplane rather than the AC direction (see SI section J). The compelling results presented in Tables 2 and 3 suggest that just extending the  $\pi$ -conjugation along one molecular axis (like our PEPF) may not lead to a champion framework where excitons can be efficiently and preferentially displaced. One would require a small intersite distance along its (major) AC direction to boost the J(AC) and a large  $\Theta$ , a feature that is commonly achieved in a rigid chromophore core.

The multilinker exciton model endowed with correlated oscillators is expected to manifest superradiance  $(\sigma_r)$ , the hallmark of the large transition dipole moment of these effective linker arrays. The experimental  $\sigma_r^{\rm ex}$  values (Table 4) highlight that the radiative rate constants in MOF-assembled

Table 4. Superradiance in csq and xly MOFs

MOF	$arphi_{ m em}$ (%)	$ au_{\mathrm{em}}$ (ns)	$k_{ m rad}$	$\sigma_{ m r}^{ m ex}~(\sigma_{ m r}^{ m pred})^a$
PCN-222(Zn)	1.6	0.70	2.28	1.48 (1.93)
NU-1000	51.0	1.00	51.00	1.24 (2.53)
SIU-100	37.0	0.89	41.60	1.66 (2.64)

 $^a\sigma_{\rm r}^{\rm ex}$  values were determined using eq 2;  $\sigma_{\rm r}^{\rm pred}=|\mu_{\rm MOF}/\mu_{\rm L}|^2$ , where the  $\mu_{\rm MOF}$  are the scaled TDDFT-calculated values presented in Table 2 and  $\mu_{\rm L}$  are the experimentally measured values from Table 1.

linkers are indeed superior to that of the corresponding solution-dissolved monomeric linkers. We note, however, that these experimental  $\sigma_{\rm r}^{\rm ex}$  values are lower than their respective predicted  $\sigma_{\rm r}^{\rm pred}$  values determined using the corrected  $\mu_{\rm cal}$  for the triangular arrays and the single linkers (Tables 1, 2). This deficiency is particularly prominent in the case of NU-1000 (~50% of the predicted value). Note, however, the predicted values do not consider all the nonradiative exciton recombination processes and their different extent as a function of the linker. For example, an ultrafast decay (relative to the IRF) such as exciton annihilation (tens of ps time scale) would not be reported in the  $\tau_{\rm em}$ , but in the  $\varphi_{\rm em}$ .

These results prompted us to check two other MOFs with symmetric topologies such as the octahedron-shaped SIU-50 and BUT-14. These scq-a MOFs are constructed with triphenylene-based linkers aligned in cofacial zigzag networks that run in a perpendicular fashion. Despite an e—h correlation seen among two or three adjacent linkers along one such zigzag chain direction, these MOFs display  $k_{\rm rad}^{\rm MOF}/k_{\rm rad}^{\rm L}\lesssim 1$ ) (see Table S6) and inferior energy transfer efficiencies compared to the csq or xly MOFs studied here.

#### CONCLUSIONS

We have established the extent and size of the molecular excitons within MOF assembled chromophoric linkers by examining the e-h correlation in the transition density of their lowest energy (optically allowed) transitions. Three csq/xly MOFs-PCN-222(Zn), NU-1000, and SIU-100-endowed with asymmetrically oriented linkers around triangular micropores and hexagonal mesopores were studied. TDDFT computations were carried out on their discrete linker arrays, taking three-linker-based triangular ensembles (closely positioned "cluster" array) and their node-sharing bis-analogues, both at the ab-plane and along the c-direction. The results highlight that proximally positioned linkers within these triangular arrays can define a unit of correlated ensembles manifesting coupled oscillators. The extent of such coupling controlled by the topology-defined distance and orientation seems to engender a transition dipole that is  $\sim 1.5$  times larger than their respective monomeric linkers. Therefore, the study underpins the importance of linker design in possessing large transition dipoles and their appropriate orientation defined by the MOF topology. These multilinker molecular excitons, endowed with coupled oscillators, can model the exciton dynamics and predict the single-step exciton hopping rate for a FRET-like migration and, therefore, should generally be used instead of an earlier single-linker localized perception. These predicted rates and the subsequent time constants match exceedingly well with the experimental hopping rate/time constants obtained from amplified emission quenching experiments (through a modified Stern-Volmer analysis with a multilinker exciton model).

This multilinker exciton model led to two fine observations: (a) modeling and predicting anisotropic exciton migration and (b) superradiance displayed by the MOF assembled linkers. The former observation suggests that the exciton can be preferentially displaced along the c-axis of these crystals and that the extent of this may depend on the linker symmetry. Therefore, porous MOF-based photochemical and photoelectrochemical developments can adopt synthetic or deposition strategies that take advantage of these findings; for example, one would need to grow free-standing (csq/xly) MOF crystallites on a catalytic substrate or electrodes. In this regard, we note that simple elongation of the linker (e.g., PEPF linker) may improve some features critical to efficient EnT but will have a ceiling defined by its length, which, in turn, measures the distance between two adjacent sites along the preferred direction. For example, with  $d_{(\overrightarrow{AC})}$  being the dominant migration direction in csq/xly MOFs, a larger value in SIU-100 has limited the hopping rate as well the extent of anisotropic exciton displacement (only ~50% of the exciton can be moved to the preferential  $\overrightarrow{AC}$  direction, compared to ~90% in NU-1000). On the other hand, superradiance has a more fundamental implication, especially on the development of superior MOF-assembled compositions: this experimentally measurable parameter can facilitate a synthetic screening for developing new compositions with a superior radiative rate constant, translating to a better exciton displacement rate.

### ASSOCIATED CONTENT

#### **5** Supporting Information

The Supporting Information is available free of charge at https://pubs.acs.org/doi/10.1021/jacs.1c11979.

Synthetic details and computational and spectroscopic data (PDF)

## AUTHOR INFORMATION

#### **Corresponding Author**

Pravas Deria — Department of Chemistry and Biochemistry, Southern Illinois University, Carbondale, Illinois 62901, United States; orcid.org/0000-0001-7998-4492; Email: pderia@siu.edu

#### **Authors**

**Sreehari Surendran Rajasree** – Department of Chemistry and Biochemistry, Southern Illinois University, Carbondale, Illinois 62901, United States

Jierui Yu – Department of Chemistry and Biochemistry, Southern Illinois University, Carbondale, Illinois 62901, United States

Saied Md Pratik — Department of Chemistry, Minnesota Supercomputing Institute, and Chemical Theory Center, University of Minnesota, Minneapolis, Minnesota 55455, United States; orcid.org/0000-0002-4900-4323

Xinlin Li – Department of Chemistry and Biochemistry, Southern Illinois University, Carbondale, Illinois 62901, United States

Rui Wang — Department of Chemistry, Northwestern University, Evanston, Illinois 60208, United States; orcid.org/0000-0001-9833-2115

Amar S. Kumbhar — Chapel Hill Analytical & Nanofabrication Laboratory, University of North Carolina—Chapel Hill, Chapel Hill, North Carolina 27599, United States; orcid.org/0000-0001-9832-0667

Subhadip Goswami — Department of Chemistry, Northwestern University, Evanston, Illinois 60208, United States; ocid.org/0000-0002-8462-9054

Christopher J. Cramer — Department of Chemistry, Minnesota Supercomputing Institute, and Chemical Theory Center, University of Minnesota, Minneapolis, Minnesota 55455, United States; Present Address: Underwriters Laboratories Inc., 333 Pfingsten Road, Northbrook, Illinois 60062, United States; orcid.org/0000-0001-5048-1859

Complete contact information is available at: https://pubs.acs.org/10.1021/jacs.1c11979

## **Author Contributions**

\*S.S.R. and J.Y. have equal contributions.

#### Notes

The authors declare no competing financial interest.

# ACKNOWLEDGMENTS

P.D. gratefully acknowledges funding from the National Science Foundation (NSF CAREER CHE-1944903). The computational research (S.M.P. and C.J.C.) was supported by the Department of Energy Office of Basic Energy Sciences, Division of Chemical Sciences, Geosciences and Biosciences, under Award DE-FG02-17ER16362. R.W. and S.G. acknowledge the support from the U.S. Department of Energy, Office of Science, Office of Basic Energy Sciences, via grant DE-FG02-87ER13808. SEM-EDS data were collected at the SIUC IMAGE center (supported by NSF grant CHE-0959568). This research used beamline 17-BM of the Advanced Photon Source, a U.S. Department of Energy (DOE) Office of Science

User Facility operated for the DOE Office of Science by Argonne National Laboratory under Contract No. DE-AC02-06CH11357.

#### REFERENCES

- (1) Gray, H. B. Powering The Planet With Solar Fuel. Nat. Chem. 2009, 1, 7.
- (2) Leem, G.; Sherman, B. D.; Burnett, A. J.; Morseth, Z. A.; Wee, K.-R.; Papanikolas, J. M.; Meyer, T. J.; Schanze, K. S. Light-Driven Water Oxidation Using Polyelectrolyte Layer-by-Layer Chromophore—Catalyst Assemblies. *ACS Energy Lett.* **2016**, *1*, 339—343.
- (3) Mulfort, K. L.; Utschig, L. M. Modular Homogeneous Chromophore–Catalyst Assemblies. Acc. Chem. Res. 2016, 49, 835–843
- (4) Kohler, L.; Mulfort, K. L. Photoinduced electron transfer kinetics of linked Ru-Co photocatalyst dyads. *J. Photochem. Photobiol., A* **2019**, 373, 59–65.
- (5) Swierk, J. R.; Mallouk, T. E. Design and Development of Photoanodes for Water-Splitting Dye-Sensitized Photoelectrochemical Cells. *Chem. Soc. Rev.* **2013**, *42*, 2357–2387.
- (6) Lebedeva, N. V.; Schmidt, R. D.; Concepcion, J. J.; Brennaman, M. K.; Stanton, I. N.; Therien, M. J.; Meyer, T. J.; Forbes, M. D. E. Structural and pH Dependence of Excited State PCET Reactions Involving Reductive Quenching of the MLCT Excited State of [Ru<sup>II</sup>(bpy)<sub>2</sub>(bpz)]<sup>2+</sup> by Hydroquinones. *J. Phys. Chem. A* **2011**, *115*, 3346–3356.
- (7) Khnayzer, R. S.; Blumhoff, J.; Harrington, J. A.; Deng, F.; Haefele, A.; Castellano, F. N. Upconversion-Powered Photoelectrochemistry. *Chem. Commun.* **2012**, *48*, 209–211.
- (8) O'Regan, B.; Grätzel, M. A Low Cost, High-Efficiency Solar Cell Based on Dye-Sensitized Colloidal TiO2 Films. *Nature* **1991**, 353, 737–740.
- (9) Williams, D. E.; Dolgopolova, E. A.; Pellechia, P. J.; Palukoshka, A.; Wilson, T. J.; Tan, R.; Maier, J. M.; Tan, R.; Greytak, A. B.; Smith, M. D.; Krause, J. A.; Shustova, N. B. A Mimic of the Green Fluorescent Protein  $\beta$ -barrel: Photophysics and Dynamics of Confined Chromophores Defined by a Rigid Porous Scaffold. *J. Am. Chem. Soc.* **2015**, 137, 2223–2226.
- (10) Williams, D. E.; Martin, C. R.; Dolgopolova, E. A.; Swifton, A.; Godfrey, D. C.; Ejegbavwo, O. A.; Pellechia, P. J.; Smith, M. D.; Shustova, N. B. Flipping the Switch: Fast Photoisomerization in a Confined Environment. *J. Am. Chem. Soc.* **2018**, *140*, 7611–7622.
- (11) Scholes, G. D.; Rumbles, G. Excitons in Nanoscale Systems. *Nat. Mater.* **2006**, *5*, 683–696.
- (12) Lim, S.-H.; Bjorklund, T. G.; Spano, F. C.; Bardeen, C. J. Exciton Delocalization and Superradiance in Tetracene Thin Films and Nanoaggregates. *Phys. Rev. Lett.* **2004**, *92*, 107402.
- (13) Scholes, G. D.; Fleming, G. R.; Olaya-Castro, A.; van Grondelle, R. Lessons from Nature about Solar Light Harvesting. *Nat. Chem.* **2011**, *3*, 763–774.
- (14) Silva, D. L.; Murugan, N. A.; Kongsted, J.; Ågren, H.; Canuto, S. Self-Aggregation and Optical Absorption of Stilbazolium Merocyanine in Chloroform. *J. Phys. Chem. B* **2014**, *118*, 1715–1725.
- (15) Stork, M.; Gaylord, B. S.; Heeger, A. J.; Bazan, G. C. Energy Transfer in Mixtures of Water-Soluble Oligomers: Effect of Charge, Aggregation, and Surfactant Complexation. *Adv. Mater.* **2002**, *14*, 361–366.
- (16) Liu, Y. H.; Zhao, J. B.; Li, Z. K.; Mu, C.; Ma, W.; Hu, H. W.; Jiang, K.; Lin, H. R.; Ade, H.; Yan, H. Aggregation and Morphology Control Enables Multiple Cases of High-Efficiency Polymer Solar Cells. *Nature Commun.* **2014**, *5*, 5293.
- (17) Tretiak, S.; Mukamel, S. Density Matrix Analysis and Simulation Of Electronic Excitations in Conjugated and Aggregated Molecules. *Chem. Rev.* **2002**, *102*, 3171–3212.
- (18) Yaghi, O. M.; O'Keeffe, M.; Ockwig, N. W.; Chae, H. K.; Eddaoudi, M.; Kim, J. Reticular Synthesis and the Design of New Materials. *Nature* **2003**, *423*, 705–714.

- (19) Horike, S.; Shimomura, S.; Kitagawa, S. Soft Porous Crystals. *Nat. Chem.* **2009**, *1*, 695–704.
- (20) Kitaura, R.; Seki, K.; Akiyama, G.; Kitagawa, S. Porous coordination-polymer crystals with gated channels specific for supercritical gases. *Angew. Chem., Int. Ed.* **2003**, 42, 428–431.
- (21) Férey, G. Hybrid Porous Solids: Past, Present, Future. Chem. Soc. Rev. 2008, 37, 191–214.
- (22) Farha, O. K.; Yazaydın, A. Ö.; Eryazici, I.; Malliakas, C. D.; Hauser, B. G.; Kanatzidis, M. G.; Nguyen, S. T.; Snurr, R. Q.; Hupp, J. T. De novo Synthesis of a Metal—Organic Framework Material Featuring Ultrahigh Surface Area and Gas Storage Capacities. *Nat. Chem.* **2010**, *2*, 944—948.
- (23) Eddaoudi, M.; Kim, J.; Rosi, N.; Vodak, D.; Wachter, J.; O'Keeffe, M.; Yaghi Omar, M. Systematic Design of Pore Size and Functionality in Isoreticular MOFs and Their Application in Methane Storage. *Science* **2002**, 295, 469–472.
- (24) Furukawa, H.; Cordova, K. E.; O'Keeffe, M.; Yaghi, O. M. The Chemistry and Applications of Metal-Organic Frameworks. *Science* **2013**, *341*, 1230444.
- (25) Kitagawa, S.; Kitaura, R.; Noro, S.-i. Functional Porous Coordination Polymers. *Angew. Chem., Int. Ed.* **2004**, *43*, 2334–2375.
- (26) Férey, G.; Mellot-Draznieks, C.; Serre, C.; Millange, F.; Dutour, J.; Surblé, S.; Margiolaki, I. A Chromium Terephthalate-Based Solid with Unusually Large Pore Volumes and Surface Area. *Science* **2005**, 309, 2040–2042.
- (27) Yu, J.; Park, J.; Van Wyk, A.; Rumbles, G.; Deria, P., Excited State Electronic Properties in Zr-based MOFs as a Function of Topological Network. *J. Am. Chem. Soc.* **2018**, *140*, 10488–10496.
- (28) Yu, J.; Anderson, R.; Li, X.; Xu, W.; Goswami, S.; Rajasree, S. S.; Maindan, K.; Gómez-Gualdrón, D. A.; Deria, P. Improving Energy Transfer within Metal—Organic Frameworks by Aligning Linker Transition Dipoles along the Framework Axis. *J. Am. Chem. Soc.* **2020**, 142, 11192—11202.
- (29) Sundström, V.; Pullerits, T. Photosynthetic Light-Harvesting: Reconciling Dynamics and Structure of Purple Bacterial LH2 Reveals Function of Photosynthetic Unit. *J. Phys. Chem. B* **1999**, *103*, 2327–2346.
- (30) Krueger, B. P.; Scholes, G. D.; Fleming, G. R. Calculation of Couplings and Energy-Transfer Pathways between the Pigments of LH2 by the ab Initio Transition Density Cube Method. *J. Phys. Chem. B* **1998**, *102*, 5378–5386.
- (31) Förster, T. Energiewanderung und Fluoreszenz. *Naturwissenschaften* **1946**, 33, 166–175.
- (32) Goswami, S.; Chen, M.; Wasielewski, M. R.; Farha, O. K.; Hupp, J. T. Boosting Transport Distances for Molecular Excitons within Photoexcited Metal—Organic Framework Films. *ACS Appl. Mater. Interfaces* **2018**, *10*, 34409—34417.
- (33) Son, H.-J.; Jin, S.; Patwardhan, S.; Wezenberg, S. J.; Jeong, N. C.; So, M.; Wilmer, C. E.; Sarjeant, A. A.; Schatz, G. C.; Snurr, R. Q.; Farha, O. K.; Wiederrecht, G. P.; Hupp, J. T. Light-Harvesting and Ultrafast Energy Migration in Porphyrin-Based Metal—Organic Frameworks. J. Am. Chem. Soc. 2013, 135, 862–869.
- (34) Since radiative decay from excited chromophores occurs through the lowest energy state, i.e.,  $S_1 \rightarrow S_0$  transition, designing a linker to boost the oscillator strength of the lowest energy vertical transition  $(S_0 \rightarrow S_1)$  should increase the overlap integral.
- (35) Feng, D.; Gu, Z.-Y.; Li, J.-R.; Jiang, H.-L.; Wei, Z.; Zhou, H.-C. Zirconium-Metalloporphyrin PCN-222: Mesoporous Metal—Organic Frameworks with Ultrahigh Stability as Biomimetic Catalysts. *Angew. Chem., Int. Ed.* **2012**, *51*, 10307–10310.
- (36) Islamoglu, T.; Otake, K.-i.; Li, P.; Buru, C. T.; Peters, A. W.; Akpinar, I.; Garibay, S. J.; Farha, O. K. Revisiting the structural homogeneity of NU-1000, a Zr-based metal—organic framework. *CrystEngComm* **2018**, *20*, 5913—5918.
- (37) Li, X.; Yu, J.; Gosztola, D. J.; Fry, H. C.; Deria, P. Wavelength-Dependent Energy and Charge Transfer in MOF: A Step toward Artificial Porous Light-Harvesting System. *J. Am. Chem. Soc.* **2019**, 141, 16849–16857.

- (38) Lu, T.; Chen, F. Multiwfn: A multifunctional wavefunction analyzer. J. Comput. Chem. 2012, 33, 580-592.
- (39) Degenerate frontier molecular orbitals leading to small transition dipoles for their respective lowest energy transitions.
- (40) Zhang, T.-G.; Zhao, Y.; Asselberghs, I.; Persoons, A.; Clays, K.; Therien, M. J. Design, Synthesis, Linear, and Nonlinear Optical Properties of Conjugated (Porphinato)zinc(II)-Based Donor—Acceptor Chromophores Featuring Nitrothiophenyl and Nitrooligothiophenyl Electron-Accepting Moieties. *J. Am. Chem. Soc.* **2005**, *127*, 9710—9720.
- (41) Angiolillo, P. J.; Uyeda, H. T.; Duncan, T. V.; Therien, M. J. Impact of Electronic Asymmetry on Photoexcited Triplet-State Spin Distributions in Conjugated Porphyrin Oligomers Probed via EPR Spectroscopy. *J. Phys. Chem. B* **2004**, *108*, 11893–11903.
- (42) Moog, R. S.; Kuki, A.; Fayer, M. D.; Boxer, S. G. Energy transport and trapping in a synthetic chlorophyllide substituted hemoglobin: orientation of the chlorophyll S1 transition dipole. *Biochemistry* **1984**, 23, 1564–1571.
- (43) Monshouwer, R.; Abrahamsson, M.; van Mourik, F.; van Grondelle, R. Superradiance and Exciton Delocalization in Bacterial Photosynthetic Light-Harvesting Systems. *J. Phys. Chem. B* **1997**, *101*, 7241–7248.
- (44) Tran-Thi, T. H.; Lipskier, J. F.; Maillard, P.; Momenteau, M.; Lopez-Castillo, J. M.; Jay-Gerin, J. P. Effect of the exciton coupling on the optical and photophysical properties of face-to-face porphyrin dimer and trimer: a treatment including the solvent stabilization effect. *J. Phys. Chem.* **1992**, *96*, 1073–1082.
- (45) This is due to the experimental difficulty in determining the extinction coefficient of the solid MOF samples.
- (46) Goswami, S.; Yu, J.; Patwardhan, S.; Deria, P.; Hupp, J. T. Light-Harvesting "Antenna" Behavior in NU-1000. ACS Energy Lett. 2021, 6, 848-853.
- (47) Yu, J.; Li, X.; Deria, P. Light-Harvesting in Porous Crystalline Compositions: Where We Stand Towards Robust Metal—Organic Frameworks. *ACS Sustainable Chem. Eng.* **2019**, *7*, 1841—1854.
- (48) Hod, I.; Bury, W.; Gardner, D. M.; Deria, P.; Roznyatovskiy, V.; Wasielewski, M. R.; Farha, O. K.; Hupp, J. T. Bias-Switchable Permselectivity and Redox Catalytic Activity of a Ferrocene-Functionalized, Thin-Film Metal—Organic Framework Compound. J. Phys. Chem. Lett. 2015, 6, 586—591.
- (49) Yu, J.; Van Wyk, A.; Smith, T.; Deria, P. Charge transfer within metal-organic frameworks: The role of polar node in the electrocatalysis and charge storage. ECS Trans. 2018, 85, 559–564.
- (50) Van Wyk, A.; Smith, T.; Park, J.; Deria, P. Charge-Transfer within Zr-Based Metal-Organic Framework: The Role of Polar Node. *J. Am. Chem. Soc.* **2018**, *140*, 2756–2760.
- (51) Deria, P.; Yu, J.; Balaraman, R. P.; Mashni, J.; White, S. N. Topology-dependent emissive properties of zirconium-based porphyrin MOFs. *Chem. Commun.* **2016**, *52*, 13031–13034.
- (52) The  $(\varphi_{\rm em}^0)/(\varphi_{\rm em}^R)$  plots against the quencher loading concentration are linear, and the  $(\varphi_{\rm em}^0)/(\varphi_{\rm em}^R)$  value for a given sample matches well with the  $\tau_0/\tau$  (see SI Appendix for discussion); this is in line with the literature report (see refs 33 and 46), suggesting a mostly dynamic quenching behavior.
- (53) The  $K_{\rm SV}$  value, presented in Figure 4, has a ~1–2% error that mostly stems from a ca. 1–3% error in QY values and 1–3% error in elemental analysis.
- (54) The absolute exciton displacement at the end of its lifetime will be 150/2 = 75 sites, and the total number of hops will be  $75^2 = 5625$ .
- (55) *csq* and related topological nets were reported with no sizable contribution from the excimer (see refs 27, 51, and 57).
- (56) Karafyllidis, I. G. Quantum transport in the FMO photosynthetic light-harvesting complex. *J. Biol. Phys.* **2017**, *43*, 239–245.
- (57) Deria, P.; Yu, J.; Smith, T.; Balaraman, R. P. Ground-State versus Excited-State Interchromophoric Interaction: Topology Dependent Excimer Contribution in Metal—Organic Framework Photophysics. J. Am. Chem. Soc. 2017, 139, 5973—5983.
- (58) Nasalevich, M. A.; Hendon, C. H.; Santaclara, J. G.; Svane, K.; van der Linden, B.; Veber, S. L.; Fedin, M. V.; Houtepen, A. J.; van

- der Veen, M. A.; Kapteijn, F.; Walsh, A.; Gascon, J. Electronic origins of photocatalytic activity in d0 metal organic frameworks. *Sci. Rep.* **2016**, *6*, 23676.
- (59) Wu, X.-P.; Gagliardi, L.; Truhlar, D. G. Cerium Metal—Organic Framework for Photocatalysis. *J. Am. Chem. Soc.* **2018**, *140*, 7904—7912.
- (60) See Figure S13 for systematic atom-numbering schemes adopted by TDDFT computations.
- (61) Tretiak, S.; Middleton, C.; Chernyak, V.; Mukamel, S. Exciton Hamiltonian for the Bacteriochlorophyll System in the LH2 Antenna Complex of Purple Bacteria. *J. Phys. Chem. B* **2000**, *104*, 4519–4528.
- (62) Mukamel, S.; Tretiak, S.; Wagersreiter, T.; Chernyak, V. Electronic Coherence and Collective Optical Excitations of Conjugated Molecules. *Science* **1997**, *277*, 781–787.
- (63) Probing larger arrays hits a computational limit, as computing 60 or so excited states with a large basis set and functional for linker arrays involving  $\gtrsim$ 600 atoms is highly expensive.
- (64) Pullerits, T.; Chachisvilis, M.; Sundström, V. Exciton Delocalization Length in the B850 Antenna of Rhodobacter sphaeroides. J. Phys. Chem. 1996, 100, 10787–10792.
- (65) The corresponding diffused-reflectance infrared Fourier-transformed spectra indicated a "locked" geometry without recruiting an aqueous ligand that would be required for any other mode where the carboxylate is attached to a single Zr site in an  $\eta^1$  or  $\eta^2$ -mode
- (66) Li, X.; Yu, J.; Lu, Z.; Duan, J.; Fry, H. C.; Gosztola, D. J.; Maindan, K.; Rajasree, S. S.; Deria, P. Photoinduced Charge Transfer with a Small Driving Force Facilitated by Exciplex-like Complex Formation in Metal—Organic Frameworks. *J. Am. Chem. Soc.* **2021**, 143, 15286—15297.
- (67) Liu, J.; Li, Z.; Zhang, X.; Otake, K.-i.; Zhang, L.; Peters, A. W.; Young, M. J.; Bedford, N. M.; Letourneau, S. P.; Mandia, D. J.; Elam, J. W.; Farha, O. K.; Hupp, J. T. Introducing Nonstructural Ligands to Zirconia-like Metal—Organic Framework Nodes To Tune the Activity of Node-Supported Nickel Catalysts for Ethylene Hydrogenation. *ACS Catal.* **2019**, *9*, 3198–3207.
- (68) In fact, SIU-100 displays a bit larger  $K_{SV}$  value.